

Electronic structure and superconductivity in bilayer $\text{La}_3\text{Ni}_2\text{O}_7$

Yuxin Wang,^{1,2} Kun Jiang,^{1,2} Ziqiang Wang,³ Fu-Chun Zhang,^{4,5} and Jiangping Hu^{1,4,6}

¹Beijing National Laboratory for Condensed Matter Physics and Institute of Physics, Chinese Academy of Sciences, Beijing 100190, China

²School of Physical Sciences, University of Chinese Academy of Sciences, Beijing 100190, China

³Department of Physics, Boston College, Chestnut Hill, MA 02467, USA

⁴Kavli Institute of Theoretical Sciences, University of Chinese Academy of Sciences, Beijing, 100190, China

⁵Collaborative Innovation Center of Advanced Microstructures, Nanjing University, Nanjing 210093, China

⁶New Cornerstone Science Laboratory, Beijing, 100190, China

(Dated: January 30, 2024)

We show that the crystal field splitting, the bilayer coupling, and electron-electron correlations all play a crucial role in creating an electronic environment similar to hole-doped cuprates for high temperature superconductivity in bilayer $\text{La}_3\text{Ni}_2\text{O}_7$ under high pressure. The previous density functional theory calculations highly underestimated the crystal field splitting and bilayer coupling. Employing the hybrid exchange-correlation functional, we show that the exchange-correlation pushes the antibonding d_{z^2} bands below the Fermi level to be fully occupied in both the low-pressure (LP) non-superconducting phase and the high-pressure (HP) phase exhibiting superconductivity. In the LP phase, the calculated Fermi surfaces and the correlation normalized band structure match well with the experimental findings at ambient pressure. Moreover, the electronic susceptibility calculated for this new band structure features nesting-induced peaks near the wave vector $Q = (\pi/2, \pi/2)$, suggesting a possible density wave instability in agreement with recent experiments. In the HP phase, an inversion symmetry between the bilayer emerges and produces a very different band structure and Fermi surface, which can be described by low-energy effective models for the inversion antisymmetric β and symmetric α bands. The β band turns out to be close to half-filling while the α band is highly overdoped. Considering the strong local Coulomb repulsion, we find a dominant pairing with B_{1g} symmetry in the β band that, upon Josephson coupling to the α band, drives a superconducting ground state with a congruent d -wave symmetry. Our results capture the essential physics of $\text{La}_3\text{Ni}_2\text{O}_7$ in both the LP and HP phases and reveal its similarity and difference from the hole-doped cuprate high-temperature superconductors.

INTRODUCTION

Being a counterpart to copper, there has long been a theoretical proposition that nickelates could harbor high-temperature superconductivity (SC) [1–5], mirroring the physics observed in the high- T_c cuprates [6–11]. However, identifying a suitable nickelate proves to be a complex challenge. Owing to sustained synthesis efforts [12–16], the manifestation of superconductivity has been successfully accomplished in thin films of the “infinite-layer” nickelates $(\text{Sr},\text{Nd})\text{NiO}_2$ in 2019 [17–19], opening the Nickel age of superconductivity [20].

Most recently, single crystals of a new type of bulk transition metal oxide $\text{La}_3\text{Ni}_2\text{O}_7$ (LNO), structurally closer to hole-doped cuprates, were successfully synthesized [21–23]. Under high pressure, a high-temperature superconducting transition $T_c \sim 80\text{K}$ was reported [21, 23–27], adding a new family to the nickelates superconductors. Following its discovery, extensive theoretical studies have been dedicated to understanding this novel material [28–38]. However, the electronic structure of LNO and its SC origin, especially the role of the e_g orbitals, are still under debate. Based on density functional theory (DFT) calculations [21, 28], it was thought that the bonding d_{z^2} band emerges as an active partially occupied band in the LNO electronic structure at high pressure. Hence, many theoretical proposals followed that the bonding d_{z^2} band may play an important role in the origin of LNO superconductivity.

In this work, we find that the crystal field splitting between the two e_g orbitals and the bilayer coupling were highly un-

derestimated in the previous DFT calculations. The important exchange correlation effects turn out to be much stronger, resulting in large splittings that push the bonding d_{z^2} bands below the Fermi level to become fully occupied. This leads to distinct new electronic structures both at ambient pressure and at high pressure for LNO. Including the multi-orbital Hubbard interactions, we find that LNO at ambient pressure harbors a density wave order close to the wave vector $Q = (\pi/2, \pi/2)$, suggesting a density wave instability in this material. At high pressure, the emergence of the inversion symmetry between the bilayer leads to a low-energy effective model including the inversion antisymmetric β and symmetric α bands. The strong electron-electron correlations can drive the near half-filled β band to generate a superconducting ground state with a congruent d -wave symmetry. This result suggests that the bilayer nickelates share a similar electronic gene of high-temperature superconductivity with the cuprates in which a near half-filled $3d_{x^2-y^2}$ orbital band is isolated near Fermi level [4, 5].

Much like the cuprates, the essential part of the LNO superconductor is the bilayer NiO_2 block [21], as illustrated in Fig. 1(a). We label them as the top (t) and bottom (b) layers. Around each Ni site, six oxygen atoms form a standard NiO_6 octahedron. The two nearest neighbor octahedrons between the two layers are corner-shared by one apical oxygen. The LNO at ambient pressure is in the Amm phase with the two octahedrons tilted in an alternating fashion, leading to four Ni atoms inside each unit cell. This low-pressure (LP) phase evolves into the high symmetry $Fmmm$ structure phase under high pressure (HP). The two octahedrons line up with two Ni

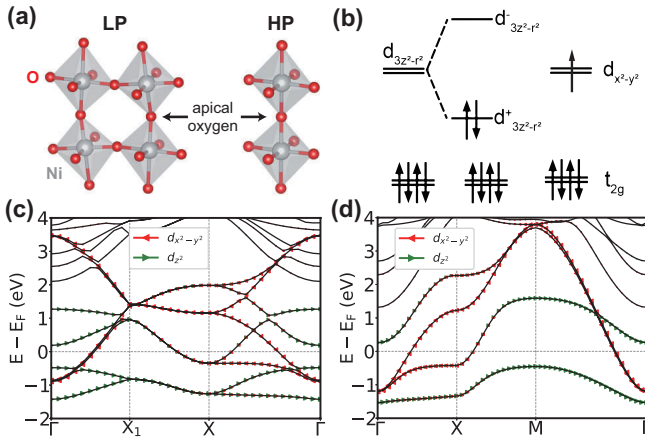


FIG. 1. (a) The essential part of the $\text{La}_3\text{Ni}_2\text{O}_7$ atomic structure is the bilayer NiO_2 plane formed by two corner-shared NiO_6 octahedrons. For the low-pressure (LP) phase, the octahedrons are tilted alternatively resulting in 4 Ni atoms in each unit cell. For the high-pressure (HP) phase, the bilayer octahedrons line up with 2 Ni atoms in each unit cell. The apical oxygens are crucial for the electronic structure. (b) The crystal field and the occupation configuration in the $(2\text{Ni})^{5+}$ state. The t_{2g} orbitals are fully occupied. The strong bilayer coupling mediated by the apical oxygen strongly splits the d_{z^2} energy level into bonding and antibonding orbitals. (c) The band structure of $\text{La}_3\text{Ni}_2\text{O}_7$ in the LP phase calculated using the HSE06 exchange-correlation functional. (d) The band structure of $\text{La}_3\text{Ni}_2\text{O}_7$ in the HP phase calculated using the HSE06 exchange-correlation functional. The labels of the high symmetry points in the Brillouin zone are given in Fig. 3(b).

atoms per unit cell as shown in Fig. 1(a) and high- T_c superconductivity emerges.

For both the Amm and $Fmmm$ structures, the octahedron crystal field splits the Ni $3d$ energy level into the standard e_g and t_{2g} complexes, as illustrated in Fig. 1(b). Counting the chemical valence in LNO, Ni is in the $(2\text{Ni})^{5+}$ state ($\text{Ni}^{2.5+}$ per-site). Hence, the $(2\text{Ni})^{5+}$ has fully occupied t_{2g} orbitals and the e_g orbitals host three electrons. Furthermore, the apical oxygen plays a crucial role for the electronic structure in LNO. The strong bilayer coupling between the d_{z^2} orbitals in the top and bottom layers is mediated by the apical oxygen and strongly splits the d_{z^2} energy level into bonding and antibonding orbitals while the $d_{x^2-y^2}$ remains nearly degenerate, as illustrated in Fig. 1(b).

ELECTRONIC STRUCTURE

The first-principle DFT calculation and its extensions are standard ways for determining the electronic structures and the crystal field energies. Various DFT calculations have been applied to finding the electronic structure of LNO [21, 28, 29, 32], even long before the discovery of superconductivity in the HP phase [39]. These calculations show that the bonding d_{z^2} bands are active and cross the Fermi level (E_F)

while the antibonding d_{z^2} bands are empty, indicating an important role of d_{z^2} orbitals. Most of the above-mentioned DFT calculations use the Generalized Gradient Approximation (GGA) exchange-correlation functional or its Perdew-Burke-Ernzerhof (PBE) version [40]. However, it is widely known that the suitable exchange-correlation functional E_{xc} is crucial for determining band gaps and binding energies [41]. For example, the GGA functional systematically underestimates band gaps of semiconductors [41, 42]. Because an accurate determination of the positions of the d_{z^2} bands is crucial for understanding the electronic structure, correlated electronic states at ambient pressure, and high- T_c superconductivity under high-pressure, as will be shown below, we will apply a more accurate exchange-correlation functional to determine the interlayer binding and crystal splitting in LNO from the DFT perspective.

Our DFT calculations employ the Vienna ab-initio simulation package (VASP) code [43] with the projector augmented wave (PAW) method [44]. The hybrid functionals that combine the Hartree-Fock (HF) and Kohn-Sham (KS) theories [45] are used here. Typically, this can be more accurate compared to the semilocal GGA method [42, 46]. Here, we implement the widely used HSE06 hybrid functional [47]. We also tested other unscreened hybrid functionals such as PBE0 [48–50] and B3LYP [51]. As discussed in the appendix, all the hybrid functionals lead to similar results. The cutoff energy for expanding the wave functions into a plane-wave basis is set to be 500 eV. The energy convergence criterion is 10^{-6} eV. All calculations are conducted using the primitive cell to save time. The Γ -centered $5 \times 5 \times 5$ and $7 \times 7 \times 7$ k-meshes are used for the LP phase and HP phase respectively. The band structures for the LP phase and HP phase using the HSE06 functional are plotted in Figs. 1(c) and (d). Compared to the PBE results (Fig. 5), the bonding d_{z^2} bands are significantly pushed below E_F by about 505 meV (Γ point in Fig. 1(c)) and 452 meV (M point in Fig. 1(d)), respectively. Both results show the crystal field splitting and bilayer coupling were highly underestimated in the PBE calculations.

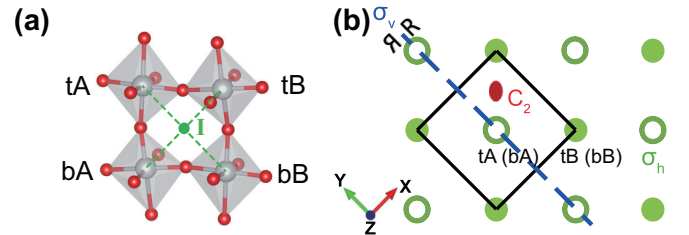


FIG. 2. (a) The essential part of the $\text{La}_3\text{Ni}_2\text{O}_7$ atomic structure in the LP phase. There are four Ni atoms per unit cell, which are labeled as tA, tB, bA, bB with t/b as layer index and A/B as sublattice index. The inversion center is indicated by I. (b) The symmetry generators in the LP phase of LNO.

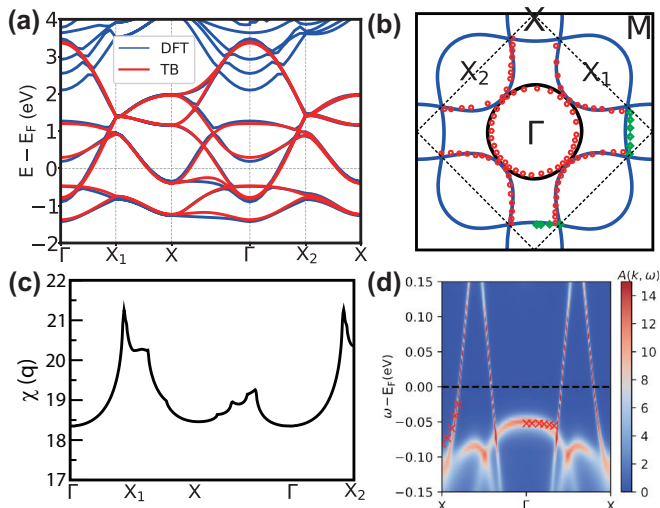


FIG. 3. (a) The DFT band structure at ambient pressure (blue lines) and the corresponding TB bands (red lines). (b) The FSs at ambient pressure from the TB bands. The red circles are experimental FSs from laser-based ARPES, while the green squares are data from synchrotron-based ARPES [52]. Notice that the Γ electron pocket nearly nests with the X_1 hole pocket at $Q = (\pi/2, \pi/2)$. (c) The spin susceptibility $\chi(q)$ is plotted as a function of q , which peaks around Q . (d) The spectral function $A(k, \omega)$ calculated using DMFT at $U = 5.5$ eV, $J_H = 0.65$ eV, and $\beta = 50$. The red crosses are experimental data from ARPES measurements [52].

LOW PRESSURE PHASE

The essential structure in the LP phase is shown in Fig. 2(a). There are four Ni atoms in each unit cell. We label them as tA, tB, bA, bB with t/b indicating the layer index and A/B the sublattice index. The inversion symmetry center I is at the center of four Ni atoms, as shown in Fig. 2(a). For the $Amam$ space group, there are three important symmetry generators, C_2 rotation, mirror plane σ_h , and the mirror plane σ_v , as illustrated in Fig. 2(b). The C_2 operation is along the z direction and exchanges A and B sites. The σ_h lies between the top and bottom layers, which maps the t and b . Combining C_2 and σ_h generates the inversion operation I . These three operations form the C_{2h} point group of the $Amam$ space group. The other four important symmetry operations in the $Amam$ space group can be generated through the σ_v along the $A - A$ direction.

Focusing on the partially occupied e_g orbitals from the DFT calculations, we use the Wannier90 code [53, 54] to fit the e_g bands and extract the tight-binding (TB) model parameters. In the following discussion, we label the $d_{x^2-y^2}$ and d_{z^2} orbital as d_x and d_z , respectively. Due to the different octahedron environments, we define every $d_{x/z}$ orbital in its local octahedra coordinates rather than the global coordinates. Because of the 4 atoms per unit cell, we obtain an 8-band TB model, whose Hamiltonian H_{LP} and hopping parameters are given in the appendix. The dispersion of the TB e_g bands is compared to the DFT calculations in Fig. 3(a), which confirms that the TB

model provides a faithful description of the low-energy electron structure.

The Fermi surfaces (FSs) of the TB model in the LP phase are plotted in Fig. 3(b). There are four FSs, one electron pocket centered around Γ , another small electron pocket around X , and two hole pockets centering around X_1 and X_2 , respectively. To directly compare to experimental findings, we also plot the FS data obtained by angle-resolved photoemission spectroscopy (ARPES) recently in Fig. 3(b) [52]. The red circles are data from laser-based ARPES and the green squares are data from synchrotron-based ARPES. Remarkably, our theoretical FSs obtained by DFT and HSE06 exchange-correlation functional show excellent agreement with the ARPES data.

Surprisingly, we find that the Γ electron FS nearly nests with the X_1 hole FS, as marked in Fig. 3(b). The nesting between electron and hole FS pockets implies divergent electronic susceptibility at the nesting wave vector and potential symmetry-breaking density wave order at low temperatures. The calculated spin susceptibility $\chi(q)$ is shown in Fig. 3(c) at different wave vectors, which indeed peaks around the near-nesting wave vector $Q = (\pi/2, \pi/2)$. This intriguing spin susceptibility feature is consistent with the recently emerged evidence for spin density wave order near Q at ambient pressure from resonant inelastic X-ray scattering (RIXS) [55], muon spin rotation (μ SR) [56], and nuclear magnetic resonance (NMR) [57] experiments below 153K [22].

To further the understanding of the electronic structure in the LP phase, we attempt a theoretical description of the band dispersions measured by ARPES [52]. To this end, it is necessary to include the electronic correlations beyond DFT, since the latter are known to produce the important renormalization of the band structure. We thus consider the multi-orbital Hubbard interactions,

$$H_I = U \sum_{i,\eta} \hat{n}_{i,\eta\uparrow} \hat{n}_{i,\eta\downarrow} + (U - 2J_H) \sum_{i,\eta \neq \eta'} \hat{n}_{i,\eta} \hat{n}_{i,\eta'} - J_H \sum_{i,\eta \neq \eta'} (\mathbf{S}_{i\eta} \cdot \mathbf{S}_{i\eta'} + d_{i,\eta\uparrow}^\dagger d_{i,\eta\downarrow}^\dagger d_{i,\eta'\uparrow} d_{i,\eta'\downarrow}) \quad (1)$$

where the $\eta = x, z$ is the orbital index. To obtain the correlation-induced band renormalization, we apply the dynamical mean field theory (DMFT) to the full Hamiltonian $H_{LP} + H_I$. Specifically, we implement the DMFT calculation using the open-source TRIQS [58] package and its continuous-time quantum Monte Carlo as an impurity solver [59]. The obtained DMFT results at $U = 5.5$ eV and $J_H = 0.65$ eV are plotted in Fig. 3(d) along the $X - \Gamma - X$ direction. The ARPES data [52] are superimposed as red crosses in Fig. 3(d), which are very well described by the DMFT results. Despite the significant correlation-induced band renormalization necessary for the remarkable agreement with ARPES, we find that correlations do not cause appreciable inter-band carrier transfer and the interacting FSs are slightly changed from Fig. 3(b). We have also performed the DFT+U calculations as discussed in the Appendix (Fig. 7), which produced large dis-

t_1^x	t_1^z	t_2^x	t_2^z	t_3^{xz}
-0.6003	-0.149	0.0391	-0.0007	0.2679
t_\perp^x	t_\perp^z	t_4^{xz}	ϵ^x	ϵ^z
0.038	-0.999	-0.072	1.2193	0.0048

TABLE I. The hopping parameters of the TB Hamiltonian $H(\mathbf{k})$ in the HP phase in unit of eV. ϵ^x, ϵ^z are site energies for Ni d_x and d_z orbitals, respectively.

agreement with the experimental results. This overall agreement with the experimental findings reassures that our new DFT electronic structure captured by the TB models plus the multi-orbital Hubbard interactions provide a reliable description for the physics of $\text{La}_3\text{Ni}_2\text{O}_7$ in its LP phase.

HIGH PRESSURE PHASE

We now turn to the HP phase and study the electronic structure and superconductivity. Under high pressure, LNO shares the same space group $Fmmm$ with the more familiar bilayer cuprate superconductor $\text{Bi}_2\text{Sr}_2\text{CaCu}_2\text{O}_x$ [60]. The symmetry discussion is thus omitted here, except noting that the inversion center is moved to the shared apical oxygen [61]. By fitting the DFT bands in Fig. 1(d), the TB model for the HP phase can be derived in the basis $(d_{ik}^x, d_{ik}^z, d_{bk}^x, d_{bk}^z)$ as

$$H_{HP}(\mathbf{k}) = \begin{pmatrix} H_t(\mathbf{k}) & H_\perp(\mathbf{k}) \\ H_\perp(\mathbf{k}) & H_b(\mathbf{k}) \end{pmatrix},$$

$$H_b(\mathbf{k}) = H_t(\mathbf{k}) = \begin{pmatrix} T_{\mathbf{k}}^x & V_{\mathbf{k}} \\ V_{\mathbf{k}} & T_{\mathbf{k}}^z \end{pmatrix}, \quad H_\perp(\mathbf{k}) = \begin{pmatrix} t_\perp^x & V'_{\mathbf{k}} \\ V'_{\mathbf{k}} & t_\perp^z \end{pmatrix}. \quad (2)$$

Here, $T_{\mathbf{k}}^{x/z} = t_1^{x/z}\gamma_k + t_2^{x/z}\alpha_k + \epsilon^{x/z}$, $V_{\mathbf{k}} = t_3^{xz}\beta_k$, $V'_{\mathbf{k}} = t_4^{xz}\beta_k$ with $\gamma_k = 2(\cos k_x + \cos k_y)$, $\alpha_k = 4 \cos k_x \cos k_y$, $\beta_k = 2(\cos k_x - \cos k_y)$. The hopping parameters and the crystal field energies are listed in Table I. Of particular importance is that the interlayer coupling $t_\perp^z = -0.999\text{eV}$ and crystal field splitting $\epsilon^x - \epsilon^z = 1.215\text{eV}$ are greatly enlarged comparing to previous TB parameters $t_\perp^z = -0.635\text{eV}$ and $\epsilon^x - \epsilon^z = 0.367\text{eV}$ [28], due to the improved treatment of the exchange-correlation functional.

The inversion eigenbasis centered at the shared apical oxygen is given by [61]

$$\psi_S^n = (d_a^n + d_b^n) / \sqrt{2} \quad (3)$$

$$\psi_A^n = (d_a^n - d_b^n) / \sqrt{2}. \quad (4)$$

They correspond to the symmetric and antisymmetric molecular orbitals that block diagonalize $H_{HP}(\mathbf{k})$ into

$$H_{HP}(\mathbf{k}) = \begin{pmatrix} H_S(\mathbf{k}) & 0 \\ 0 & H_A(\mathbf{k}) \end{pmatrix}, \quad (5)$$

where $H_{S/A}(\mathbf{k})$ takes the same form as $H_{t/b}(\mathbf{k})$ in Eq. (2). The TB electronic structure is plotted in Fig. 4(a), which is divided

into two ψ_S bands (black dash lines) and two ψ_A bands (blue dash lines). There are *two bands* crossing E_F , which are labeled by α, β , which are separated from an unoccupied δ band and a fully occupied γ band. The FSs consist of one electron pocket (α band) around the Γ point and one hole pocket (β band) around the M points in the Brillouin zone as shown in Fig. 4(b).

We start with the antisymmetric ψ_A bands. Since the upper δ band is empty, we focus on the antisymmetric β band, which is partially occupied by 0.73 electrons or 0.27 holes, and is close to half-filling. The dispersion of the β band can be described by $t\gamma_k + t'\alpha_k + t''\gamma_{2k}$ with the effective nearest neighbor (t), second and third neighbor hoppings (t', t'') given in the appendix. It is plotted as the red line in Fig. 4(a) and contributes to the red-lined β -FS in Fig. 4(b). It is important to note that this β FS is very close to that of hole-doped cuprates. The β band plays a similar role of Zhang-Rice singlets in cuprates [61, 62]. We can introduce a large ‘‘on-site’’ Coulomb repulsion for the molecule β band, here a ‘‘site’’ means a molecule site consisting of two crystal sites with one in the top and one in the bottom layer shared through the apical oxygen. As the β band is hole-doped away from half-filling, we can apply the one band t - J model captured the physics of strong local repulsion [6],

$$H_\beta = \sum_{ij} t_{ij} \hat{P} \psi_{\beta, i\sigma}^\dagger \psi_{\beta, j\sigma} \hat{P} + \sum_{\langle ij \rangle} J (\mathbf{S}_i \cdot \mathbf{S}_j - \frac{1}{4} n_i n_j). \quad (6)$$

Here the projection operator \hat{P} is for removing the double occupancy, J is the superexchange interaction, and summation over repeated indices is used.

Then, we apply a slave-boson mean-field study of the t - J model by writing $\psi_{\beta, i\sigma} = b_i^\dagger f_{i\sigma}$, where b_i is a slave-boson keeping track of empty sites and $f_{i\sigma}$ is a spin-1/2 fermion keeping track of singly-occupied sites [6, 63]. The mean-field nearest neighbor bond and spin-singlet pairing order parameters $\chi_{ij} = \langle f_{i\sigma}^\dagger f_{j\sigma} \rangle$ and $\Delta_{ij} = \langle f_{i\uparrow} f_{j\downarrow} - f_{i\downarrow} f_{j\uparrow} \rangle$ are self-consistently calculated. The bosons b_i are condensed to take expectation values $\sqrt{x_i}$, where x_i is the hole doping concentration at the molecule site i . Choosing the homogeneous solution with $\chi_{ij} = \chi$, $x_i = x$, we find that the B_{1g} pairing ansatz, with $\Delta_x = \Delta$ and $\Delta_y = -\Delta$ for bonds along x and y directions, is the ground state as in the cuprates [6, 64]. The mean-field order parameters are self-consistently calculated and plotted in Fig. 4(c), as a function of the hole doping level x . For the β band with a doping around $x = 0.27$ (indicated by the blue star in Fig. 4(c)), we obtain $\chi = 0.36$ and $\Delta = 0.079$. Thus, independent of the precise value of x , the close to half-filled β band plays the leading role in producing the high- T_c superconductivity in LNO.

Next, we consider the inversion symmetric ψ_S bands. The dispersion of the α band can also be fitted by a TB band $t\gamma_k + t'\alpha_k + t''\gamma_{2k}$ (green line in Fig. 4(a)) with the hopping parameters given in the Appendix. It has an electron filling ~ 0.27 and the corresponding FS is plotted as the green circle in Fig. 4(b). Applying a similar slave-boson mean field theory to the α band does not lead to sizeable pairing, since the α

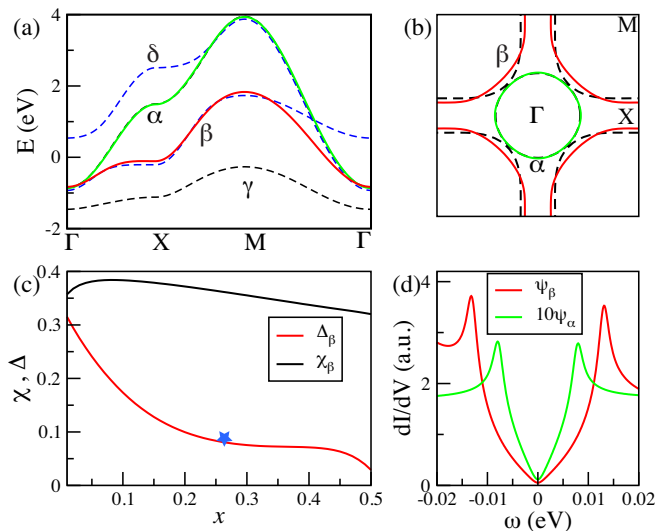


FIG. 4. (a) The TB band dispersions in the HP phase of LNO. The antisymmetric ψ_A bands are plotted in blue dashed lines. The symmetric ψ_S bands are plotted in black dashed lines. We fit the β band and α band with the red solid line and green solid line using the single-band $t - t' - t''$ model. (b) The FSs for the β band and α band from the TB and fitted models in the first Brillouin zone. (c) The calculated mean-field order parameters χ_β and Δ_β as a function of hole doping x in the β band. The exchange coupling is $J = 0.12$ eV. The blue star marks $x = 0.27$. (d) The tunneling density of states in the congruent d -wave pairing phase. The spin-orbital exchange coupling is $J_{SA} = 0.05$ eV. The green line from the ψ_α band is magnified by a factor of 10 for visualization.

band is highly overdoped from half-filling. The corresponding density of state (DOS) is relatively small compared to the strongly renormalized antisymmetric β band that dominates the DOS of the whole system. Hence, it is important to consider the coupling between the symmetric and antisymmetric sectors for the superconducting state of LNO.

Microscopically, although the inversion symmetry decouples the ψ_S and ψ_A bands for the single-particle excitations, the Coulomb interactions couple the two sectors [61]. For our consideration, the most important symmetry-allowed coupling is the spin-orbital exchange interaction [65, 66],

$$H_{SAS} = J_{SA}(\hat{\Delta}_{S\alpha}^\dagger \hat{\Delta}_{A\beta} + h.c.), \quad (7)$$

which serves as an effective Josephson coupling between the pairing order parameters in the symmetric and antisymmetric sectors. Choosing a moderate $J_{SA} = 0.05$ eV, we calculate the pairing order parameters self-consistently by solving for the ground state of $H_\beta^{MF} + H_\alpha^{MF} + H_{SAS}$ [61]. Intriguingly, the B_{1g} superconducting state in the β band, through the coupling J_{SA} , drives a congruent B_{1g} pairing state in the symmetric α bands. Specifically, all order parameters have a d -wave symmetry with amplitudes $(\Delta_\beta; \Delta_\alpha) = (0.099; 0.008)$. The calculated tunneling DOS plotted in Fig. 4(d) shows that the contribution from the β band dominates and the spectral weight from the ψ_α bands is magnified by a factor of 10 for visual-

ization. As clearly seen in Fig. 4(d), the energy gap from the α band is around 8 meV. The DOS reveals a gap around 13.2 meV from the β band. We thus conclude that exchange coupling the strongly correlated β band to the weakly correlated α with a large carrier density produces a congruent d -wave pairing state with boosted pairing energy gap and enhanced high- T_c superconductivity, which can be a novelty of LNO under pressure.

SUMMARY AND DISCUSSION

In summary, we presented a systematic study on the correlated electronic structure and superconductivity in bilayer $\text{La}_3\text{Ni}_2\text{O}_7$. Utilizing advanced exchange-correlation functionals, new electronic structures of LNO have been identified from the DFT calculations for both the LP and HP phases. In sharp contrast to previous GGA functional results, the bilayer coupling and the e_g crystal fields are greatly enhanced. This enhancement pushes the bonding d_{z^2} band down to lie below the Fermi level. The obtained Fermi surface structure in the LP phase matches well the recent ARPES measurements performed at ambient pressure. Moreover, the calculated spin susceptibility exhibits near nesting peak structures around the wave vector $Q = (\pi/2, \pi/2)$, which is consistent with recent RIXS resolved magnon dispersion and additional evidence from the μSR and NMR experiments. Beyond the DFT calculation, we apply the DMFT to study the effects of multi-orbital Hubbard interactions using the DFT derived tight-binding models in the low-pressure phase. The renormalized band structures quantitatively match the bands detected by the ARPES-measured spectral functions. Therefore, our new TB model plus multi-orbital Hubbard interactions provide a faithful description of the electronic structure in LNO.

In the HP phase, we study the nature of the unconventional superconductivity. Because of the strong interlayer hybridization, the unoccupied bonding and fully occupied antibonding d_{z^2} bands are dormant and the low-energy physics is determined by the partially filled β and α bands, which correspond to the symmetric and antisymmetric molecular orbitals, respectively. We then study the physics of strong local coulomb repulsion at the molecular site consisting of two crystal sites with one in the top and one in the bottom layer. The Hamiltonian for the antisymmetric states describes a moderately hole-doped t - J model on a square lattice, which gives rise to d -wave superconductivity, similar to the theoretical description of d -wave superconductivity in hole-doped high- T_c cuprates [7] and the $\text{LaNiO}_3/\text{LaMO}_3$ superlattices [3]. The symmetric α band, on the other hand, is lightly filled by electrons or heavily hole-doped from half-filling, and as such does not lead to sizable superconducting pairing. We argued by explicit calculations that the spin-orbital exchange coupling between the symmetric and antisymmetric sectors leads to an effective Josephson coupling, which drives a congruent d -wave pairing state with boosted superconducting energy gap and en-

hanced transition temperature T_c , beyond those of the typical single-layer cuprates. Since both β and α bands are formed through the apical oxygen, the apical oxygen vacancies in LNO play a similar role of in-plane vacancies in cuprates. Therefore, the apical oxygen vacancies are crucial for the high-temperature superconductivity in LNO [67]. While completing our manuscript, we became aware of a recent work [68], pointing out that LNO has similar Fermi surface structures with three classes of cuprates, which agrees well with the new band structure uncovered here. It is thus conceivable that the HP phase of $\text{La}_3\text{Ni}_2\text{O}_7$ constitutes a much needed and original realization of the essential physics of hole-doped cuprate high- T_c superconductors.

Acknowledgement

We acknowledge the support by the Ministry of Science and Technology (Grant No. 2022YFA1403900), the National Natural Science Foundation of China (Grant No. NSFC-11888101, No. NSFC-12174428, No. NSFC-11920101005), the Strategic Priority Research Program of the Chinese Academy of Sciences (Grant No. XDB28000000, XDB33000000), the New Cornerstone Investigator Program, and the Chinese Academy of Sciences Project for Young Scientists in Basic Research (2022YSBR-048). Z.W. is supported by the U.S. Department of Energy, Basic Energy Sciences Grant No. DE-FG02-99ER45747.

APPENDIX

Exchange-correlation functional, GGA, and Hybrid functional

DFT is a powerful computational method to investigate the electronic structure of solids. The basic computational methods behind DFT calculations are the Kohn-Sham equations, which provide a systematic way of mapping the many-body system onto a single-body problem [41]. More precisely, the total energy of the system in Kohn-Sham theory is written as a functional of electron density $\rho(\mathbf{r})$,

$$E[\rho] = T_s[\rho] + \int d\mathbf{r} v_{ext}(\mathbf{r})\rho(\mathbf{r}) + E_H[\rho] + E_{xc}[\rho] \quad (8)$$

The $T_s[\rho]$ is the Kohn-Sham kinetic energy, $v_{ext}(\mathbf{r})$ is the external potential like the electron-nuclei interaction, and $E_H[\rho]$ is the Hartree energy. The $E_{xc}[\rho]$ is the exchange-correlation functional. T_s , v_{ext} , $E_H[\rho]$ can be straightforwardly calculated. The only unknown in Kohn-Sham theory is the exchange-correlation functional E_{xc} [41, 46]. Developing a precise E_{xc} is one central goal in the DFT framework. Hence, implementing a precise E_{xc} is a crucial step for band structure calculation. The most commonly used E_{xc} in solid-state physics is the GGA or its PBE version [40]. The PBE band structures of LNO in the LP and HP phases are plotted in Fig. 5. In both

cases, the bonding d_z bands cross the Fermi level, which is due to the underestimated exchange correlations.

Going beyond GGA, a more advanced exchange-correlation functional E_{xc} is the hybrid functional. The exchange part or correlation part of E_{xc} is a linear combination of the Hartree-Fock (HF) exchange and semilocal potential such as GGA. The hybrid functionals can be divided into two families according to the interelectronic range at which the HF exchange is applied: screened (range-separated) and unscreened. The screened hybrid functional like sophisticated HSE06 which mixes GGA and HF in the short-range exchange energy is often used in solid state calculations. It provides great accuracy for band gaps [42]. There are also other unscreened hybrid functionals like the PBE0 [48–50] and B3LYP [51], which have slower convergence than HSE06 and also been tested. PBE0 is similar to HSE06 but mixes both the short-range and the long-range contributions. B3LYP mixes LDA, HF, and Becke88 in the exchange energy. The correlation energy is also a mixture of LYP and VWN3. The PBE0 and B3LYP band structures are shown in Fig. 6, which are similar to HSE06 in the main text.

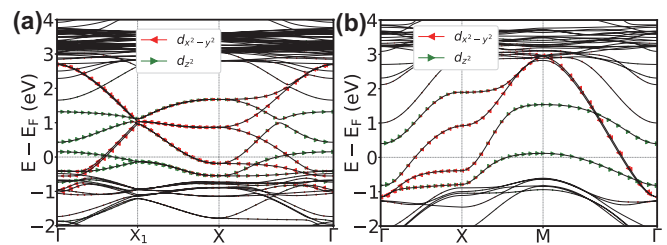


FIG. 5. LNO electronic structure obtained using GGA exchange-correlation functional. (a) PBE functional calculated band dispersions in the LP phase. (b) PBE functional calculated band dispersions in the HP phase.

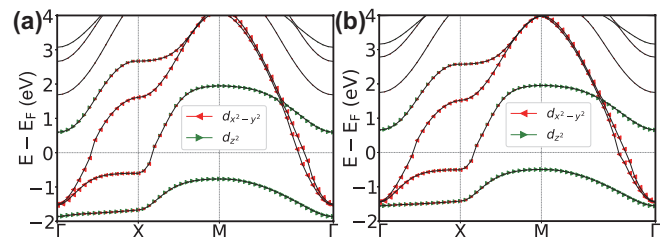


FIG. 6. LNO band structure calculated using the hybrid functional. (a) PBE0 functional calculated band dispersions in the HP phase. (b) B3LYP functional calculated band dispersions in the HP phase.

DFT+U and DMFT

Although the hybrid functional provides an accurate description of band structure, the local Hubbard interactions

beyond DFT should be treated using other many-body techniques. The DFT+U is one convenient approach [41]. However, DFT+U only shifts the crystal field splitting without renormalizing the hopping parameters or the bandwidths. In previous works, it was proposed that DFT+U (using PBE functional) can capture the ARPES measurements of the band dispersion in ambient pressure [52]. We calculate the band structure of the LP phase using the simplified rotation invariant approach to the DFT+U introduced by Dudarev *et al.* [69]. As shown in Fig. 7, the DFT+U results with $U=4\text{eV}$ deviate significantly from the ARPES measurement.

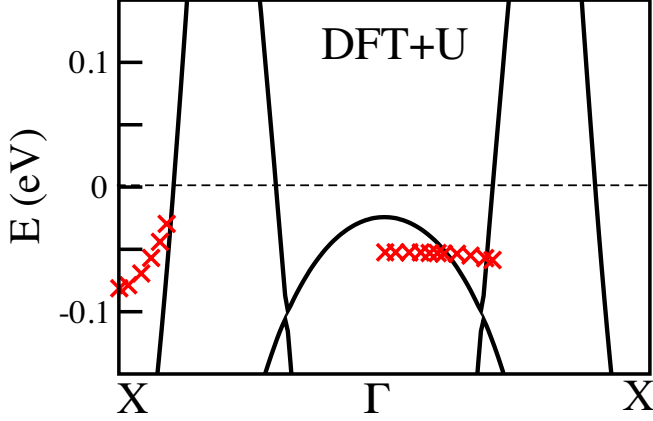


FIG. 7. The DFT+U band dispersion using PBE functional at $U = 4$ eV. The calculated band dispersion cannot describe the experiment data (red crosses) owing to the missing additional renormalization effects in DFT+U.

In the main text, we presented a DMFT study of the spectral function in the LP phase. The basic assumption of DMFT is that the self-energy only depends on the frequency $\Sigma(\omega)$. We use the open-source TRIQS DMFT package [58] and its CTQMC solver [59]. In the LP phase, there are four Ni atoms. To simplify our discussion, we treat them equally in the DMFT calculation. During each DMFT self-consistent calculation, a 40×40 Brillouin zone mesh is used for the lattice Green's function calculation.

Hamiltonian and Tight-binding parameters

The TB model for LNO in the LP phase can be derived in the basis (the spin index is omitted here) $(d_{iA\mathbf{k}}^x, d_{iA\mathbf{k}}^z, d_{iB\mathbf{k}}^x, d_{iB\mathbf{k}}^z, d_{bA\mathbf{k}}^x, d_{bA\mathbf{k}}^z, d_{bB\mathbf{k}}^x, d_{bB\mathbf{k}}^z)$ as

$$H_{LP}(\mathbf{k}) = \begin{pmatrix} H_t(\mathbf{k}) & H_{\perp}(\mathbf{k}) \\ H_{\perp}^{\dagger}(\mathbf{k}) & H_b(\mathbf{k}) \end{pmatrix}, \quad (9)$$

where $H_b(\mathbf{k}) = H_t(\mathbf{k})$ and $H_{\perp}(\mathbf{k}) = H_{\perp}^{\dagger}(\mathbf{k})$. They take the structures of

$$H_t(\mathbf{k}) = \begin{pmatrix} H_{11}(\mathbf{k}) & 0 & H_{13}(\mathbf{k}) & H_{14}(\mathbf{k}) \\ 0 & H_{22}(\mathbf{k}) & H_{14}(\mathbf{k}) & H_{24}(\mathbf{k}) \\ H_{13}^*(\mathbf{k}) & H_{14}^*(\mathbf{k}) & H_{11}(\mathbf{k}) & 0 \\ H_{14}^*(\mathbf{k}) & H_{24}^*(\mathbf{k}) & 0 & H_{22}(\mathbf{k}) \end{pmatrix}, \quad (10)$$

$$H_{\perp}(\mathbf{k}) = \begin{pmatrix} t_{\perp}^x & 0 & 0 & H_{18}(\mathbf{k}) \\ 0 & t_{\perp}^z & H_{18}(\mathbf{k}) & 0 \\ 0 & H_{18}^*(\mathbf{k}) & t_{\perp}^x & 0 \\ H_{18}^*(\mathbf{k}) & 0 & 0 & t_{\perp}^z \end{pmatrix}, \quad (11)$$

with $H_{11/22}(\mathbf{k}) = \epsilon^{x/z} + 2(t_2^{x/z} \cos k_X + t_2^{x/z} \cos k_Y) + 4t_5^{x/z} \cos k_X \cos k_Y$, $H_{13/24}(\mathbf{k}) = 2 \cos \frac{1}{2} k_X (t_1^{x/z} e^{i\frac{1}{2} k_Y} + t_1'^{x/z} e^{-i\frac{1}{2} k_Y})$ and $H_{14/18}(\mathbf{k}) = 2i \sin \frac{1}{2} k_X (t_3/4^{xz} e^{i\frac{1}{2} k_Y} - t_3/4'^{xz} e^{-i\frac{1}{2} k_Y})$. Here, $k_X = k_x + k_y$ and $k_Y = -k_x + k_y$ are vectors defined in the enlarged unit cell. The hopping parameters in the TB model for the bilayer eight-orbital model in the LP phase are listed in Tab. II. The corresponding schematic illustration is shown in Fig. 8. We add the third nearest neighbor hopping parameters $t_5^{x/z}$ in the diagonal terms in order to achieve a better fitting.

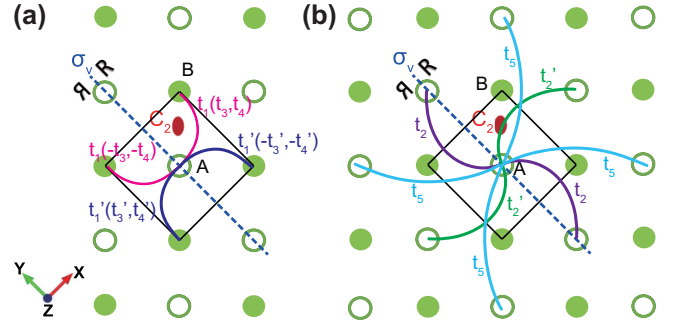


FIG. 8. (a), (b) The hopping parameters used in TB of LP LNO.

t_1^x	$t_1^{x'}$	t_1^z	$t_1^{z'}$	t_2^x	$t_2^{x'}$	t_2^z	$t_2^{z'}$	t_3^{xz}
-0.519	-0.525	-0.123	-0.104	0.069	0.08	-0.019	-0.018	0.271
t_3^{xz}	t_4^{xz}	t_4^{xz}	t_5^x	t_5^z	t_{\perp}^x	t_{\perp}^z	ϵ^x	ϵ^z
0.258	-0.033	-0.026	-0.051	-0.013	0.017	-0.835	1.196	0.039

TABLE II. Hopping parameters in the TB Hamiltonian (unit here is eV) in the LP phase. ϵ^x, ϵ^z are site energies for Ni $d_{x^2-y^2}$ and $d_{3z^2-r^2}$ orbitals, respectively.

In the main text, the TB model Hamiltonian in the HP phase is discussed. Using the molecular ψ_S and ψ_A orbitals, $H_{HP}(\mathbf{k})$ is block-diagonalized into

$$H_{HP}(\mathbf{k}) = \begin{pmatrix} H_S(\mathbf{k}) & 0 \\ 0 & H_A(\mathbf{k}) \end{pmatrix}, \quad (12)$$

where $H_S(\mathbf{k})$, $H_A(\mathbf{k})$ have the same structure as $H_I(\mathbf{k})$

$$H_{S/A}(\mathbf{k}) = \begin{pmatrix} T_{\mathbf{k}}^x & V_{\mathbf{k}} \\ V_{\mathbf{k}} & T_{\mathbf{k}}^z \end{pmatrix}, \quad (13)$$

with $T_{\mathbf{k}}^{x/z} = t_1^{x/z}\gamma_k + t_2^{x/z}\alpha_k + \epsilon^{x/z}$, $V_{\mathbf{k}} = t_3^{xz}\beta_k$. The hopping parameters and site energies are listed in Tab. III.

sector	t_1^x	t_1^z	t_2^x	t_2^z	t_3^{xz}	ϵ^x	ϵ^z
ψ_S	-0.6003	-0.149	0.0391	-0.0007	0.1959	1.2573	-0.9942
ψ_A	-0.6003	-0.149	0.0391	-0.0007	0.3399	1.1813	1.0038

TABLE III. TB hopping parameters in the basis of ψ_S and ψ_A and site energies in the HP phase of LNO.

For the fitting of the β band, we use up to the third nearest neighbor hopping in the TB model on the square lattice $t\gamma_k + t'\alpha_k + t''\gamma_{2k}$. The parameters are $t = -0.3326\text{eV}$, $t' = 0.07633\text{eV}$, $t'' = -0.05\text{eV}$. We also fit the α band with the parameters $t = -0.6\text{eV}$, $t' = 0.0065\text{eV}$, $t'' = -0.01\text{eV}$.

- [1] V. I. Anisimov, D. Bukhvalov, and T. M. Rice, "Electronic structure of possible nickelate analogs to the cuprates," *Phys. Rev. B* **59**, 7901–7906 (1999).
- [2] K.-W. Lee and W. E. Pickett, "Infinite-layer LaNiO₂: Ni¹⁺ is not Cu²⁺," *Phys. Rev. B* **70**, 165109 (2004).
- [3] Ji ǝ Chaloupka and Giniyat Khaliullin, "Orbital Order and Possible Superconductivity in LaNiO₃/LaMO₃ Superlattices," *Phys. Rev. Lett.* **100**, 016404 (2008).
- [4] Jiangping Hu, Congcong Le, and Xianxin Wu, "Predicting unconventional high-temperature superconductors in trigonal bipyramidal coordinations," *Phys. Rev. X* **5**, 041012 (2015).
- [5] Jiangping Hu, "Identifying the genes of unconventional high temperature superconductors," *Science Bulletin* **61**, 561 (2016).
- [6] Patrick A. Lee, Naoto Nagaosa, and Xiao-Gang Wen, "Doping a mott insulator: Physics of high-temperature superconductivity," *Rev. Mod. Phys.* **78**, 17–85 (2006).
- [7] B. Keimer, S. A. Kivelson, M. R. Norman, S. Uchida, and J. Zaanen, "From quantum matter to high-temperature superconductivity in copper oxides," *Nature* **518**, 179–186 (2015).
- [8] Y. Maeno, H. Hashimoto, K. Yoshida, S. Nishizaki, T. Fujita, J. G. Bednorz, and F. Lichtenberg, "Superconductivity in a layered perovskite without copper," *Nature* **372**, 532–534 (1994).
- [9] Yoichi Kamihara, Takumi Watanabe, Masahiro Hirano, and Hideo Hosono, "Iron-Based Layered Superconductor La[O_{1-x}F_x]FeAs (x=0.05-0.12) with T_c =26K," *Journal of the American Chemical Society* **130**, 3296–3297 (2008).
- [10] Hiroki Takahashi, Kazumi Igawa, Kazunobu Arii, Yoichi Kamihara, Masahiro Hirano, and Hideo Hosono, "Superconductivity at 43 K in an iron-based layered compound LaO_{1-x}F_xFeAs," *Nature* **453**, 376–378 (2008).
- [11] Johnpierre Paglione and Richard L. Greene, "High-temperature superconductivity in iron-based materials," *Nature Physics* **6**, 645–658 (2010).
- [12] Michel Crespin, Pierre Levitz, and Lucien Gatineau, "Reduced forms of LaNiO₃ perovskite. Part I.—Evidence for new phases: La₂Ni₂O₅ and LaNiO₂," *J. Chem. Soc., Faraday Trans. 2* **79**, 1181–1194 (1983).
- [13] Martha Greenblatt, "Ruddlesden-Popper Ln_{n+1}Ni_nO_{3n+1} nickelates: structure and properties," *Current Opinion in Solid State and Materials Science* **2**, 174–183 (1997).
- [14] M. A. Hayward, M. A. Green, M. J. Rosseinsky, and J. Sloan, "Sodium Hydride as a Powerful Reducing Agent for Topotactic Oxide Deintercalation: Synthesis and Characterization of the Nickel(I) Oxide LaNiO₂," *Journal of the American Chemical Society* **121**, 8843–8854 (1999).
- [15] M. Crespin, O. Isnard, F. Dubois, J. Choisnet, and P. Odier, "LaNiO₂: Synthesis and structural characterization," *Journal of Solid State Chemistry* **178**, 1326–1334 (2005).
- [16] Masanori Kawai, Kazuya Matsumoto, Noriya Ichikawa, Masachiro Mizumaki, Osami Sakata, Naomi Kawamura, Shigeru Kimura, and Yuichi Shimakawa, "Orientation Change of an Infinite-Layer Structure LaNiO₂ Epitaxial Thin Film by Annealing with CaH₂," *Crystal Growth & Design* **10**, 2044–2046 (2010).
- [17] Danfeng Li, Kyuho Lee, Bai Yang Wang, Motoki Osada, Samuel Crossley, Hye Ryoung Lee, Yi Cui, Yasuyuki Hikita, and Harold Y. Hwang, "Superconductivity in an infinite-layer nickelate," *Nature* **572**, 624–627 (2019).
- [18] Motoki Osada, Bai Yang Wang, Kyuho Lee, Danfeng Li, and Harold Y. Hwang, "Phase diagram of infinite layer praseodymium nickelate Pr_{1-x}Sr_xNiO₂ thin films," *Phys. Rev. Mater.* **4**, 121801 (2020).
- [19] Danfeng Li, Bai Yang Wang, Kyuho Lee, Shannon P. Harvey, Motoki Osada, Berit H. Goodge, Lena F. Kourkoutis, and Harold Y. Hwang, "Superconducting Dome in Nd_{1-x}Sr_xNiO₂ Infinite Layer Films," *Phys. Rev. Lett.* **125**, 027001 (2020).
- [20] Michael R. Norman, "Entering the Nickel Age of Superconductivity," *Physics* **13**, 85 (2020).
- [21] Hualei Sun, Mengwu Huo, Xunwu Hu, Jingyuan Li, Zengjia Liu, Yifeng Han, Lingyun Tang, Zhongquan Mao, Pengtao Yang, Bosen Wang, Jinguang Cheng, Dao-Xin Yao, Guang-Ming Zhang, and Meng Wang, "Signatures of superconductivity near 80 K in a nickelate under high pressure," *Nature* **621**, 493–498 (2023).
- [22] Zengjia Liu, Hualei Sun, Mengwu Huo, Xiaoyan Ma, Yi Ji, Enkui Yi, Lisi Li, Hui Liu, Jia Yu, Ziyou Zhang, Zhiqiang Chen, Feixiang Liang, Hongliang Dong, Hanjie Guo, Dingyong Zhong, Bing Shen, Shiliang Li, and Meng Wang, "Evidence for charge and spin density waves in single crystals of La₃Ni₂O₇ and La₃Ni₂O₆," *Science China Physics, Mechanics & Astronomy* **66**, 217411 (2022).
- [23] Gang Wang, Ningning Wang, Yuxin Wang, Lifeng Shi, Xiaoling Shen, Jun Hou, Hanming Ma, Pengtao Yang, Ziyi Liu, Hua Zhang, Xiaoli Dong, Jianping Sun, Bosen Wang, Kun Jiang, Jiangping Hu, Yoshiya Uwatoko, and Jinguang Cheng, "Observation of high-temperature superconductivity in the high-pressure tetragonal phase of La₂PrNi₂O_{7-δ}," *arXiv e-prints*, [arXiv:2311.08212](https://arxiv.org/abs/2311.08212) (2023), [arXiv:2311.08212](https://arxiv.org/abs/2311.08212) [cond-mat.supr-con].
- [24] J. Hou, P. T. Yang, Z. Y. Liu, J. Y. Li, P. F. Shan, L. Ma, G. Wang, N. N. Wang, H. Z. Guo, J. P. Sun, Y. Uwatoko, M. Wang, G. M. Zhang, B. S. Wang, and J. G. Cheng, "Emergence of high-temperature superconducting phase in the pressurized La₃Ni₂O₇ crystals," *arXiv e-prints*, [arXiv:2307.09865](https://arxiv.org/abs/2307.09865) (2023), [arXiv:2307.09865](https://arxiv.org/abs/2307.09865) [cond-mat.supr-con].
- [25] Yanan Zhang, Dajun Su, Yanen Huang, Hualei Sun, Mengwu Huo, Zhaoyang Shan, Kaixin Ye, Zihan Yang, Rui Li, Michael Smidman, Meng Wang, Lin Jiao, and Huiqiu Yuan, "High-temperature superconductivity with zero-resistance and strange metal behavior in La₃Ni₂O₇," *arXiv e-prints*, [arXiv:2307.14819](https://arxiv.org/abs/2307.14819) (2023), [arXiv:2307.14819](https://arxiv.org/abs/2307.14819) [cond-mat.supr-con].

- [26] Gang Wang, Ningning Wang, Jun Hou, Liang Ma, Lifen Shi, Zhian Ren, Yadong Gu, Xiaoling Shen, Hanming Ma, Pengtao Yang, Ziyi Liu, Haizhong Guo, Jianping Sun, Guangming Zhang, Jiaqiang Yan, Bosen Wang, Yoshiya Uwatoko, and Jinguang Cheng, “Pressure-induced superconductivity in polycrystalline $\text{La}_3\text{Ni}_2\text{O}_7$,” [arXiv e-prints](#) , [arXiv:2309.17378 \(2023\)](#), [arXiv:2309.17378 \[cond-mat.supr-con\]](#).
- [27] Yazhou Zhou, Jing Guo, Shu Cai, Hualei Sun, Pengyu Wang, Jinyu Zhao, Jinyu Han, Xintian Chen, Qi Wu, Yang Ding, Meng Wang, Tao Xiang, Ho-kwang Mao, and Liling Sun, “Evidence of filamentary superconductivity in pressurized $\text{La}_3\text{Ni}_2\text{O}_7$ single crystals,” [arXiv e-prints](#) , [arXiv:2311.12361 \(2023\)](#), [arXiv:2311.12361 \[cond-mat.supr-con\]](#).
- [28] Zhihui Luo, Xunwu Hu, Meng Wang, Wéi Wú, and Dao-Xin Yao, “Bilayer two-orbital model of $\text{La}_3\text{Ni}_2\text{O}_7$ under pressure,” [arXiv e-prints](#) , [arXiv:2305.15564 \(2023\)](#), [arXiv:2305.15564 \[cond-mat.supr-con\]](#).
- [29] Yang Zhang, Ling-Fang Lin, Adriana Moreo, and Elbio Dagotto, “Electronic structure, orbital-selective behavior, and magnetic tendencies in the bilayer nickelate superconductor $\text{La}_3\text{Ni}_2\text{O}_7$ under pressure,” [arXiv e-prints](#) , [arXiv:2306.03231 \(2023\)](#), [arXiv:2306.03231 \[cond-mat.supr-con\]](#).
- [30] Qing-Geng Yang, Da Wang, and Qiang-Hua Wang, “Possible s_{\pm} -wave superconductivity in $\text{La}_3\text{Ni}_2\text{O}_7$,” [arXiv e-prints](#) , [arXiv:2306.03706 \(2023\)](#), [arXiv:2306.03706 \[cond-mat.supr-con\]](#).
- [31] Hirofumi Sakakibara, Naoya Kitamine, Masayuki Ochi, and Kazuhiko Kuroki, “Possible high T_c superconductivity in $\text{La}_3\text{Ni}_2\text{O}_7$ under high pressure through manifestation of a nearly-half-filled bilayer Hubbard model,” [arXiv e-prints](#) , [arXiv:2306.06039 \(2023\)](#), [arXiv:2306.06039 \[cond-mat.supr-con\]](#).
- [32] Yuhao Gu, Congcong Le, Zhesen Yang, Xianxin Wu, and Jiangping Hu, “Effective model and pairing tendency in bilayer Ni-based superconductor $\text{La}_3\text{Ni}_2\text{O}_7$,” [arXiv e-prints](#) , [arXiv:2306.07275 \(2023\)](#), [arXiv:2306.07275 \[cond-mat.supr-con\]](#).
- [33] Yang Shen, Mingpu Qin, and Guang-Ming Zhang, “Effective bi-layer model Hamiltonian and density-matrix renormalization group study for the high- T_c superconductivity in $\text{La}_3\text{Ni}_2\text{O}_7$ under high pressure,” [arXiv e-prints](#) , [arXiv:2306.07837 \(2023\)](#), [arXiv:2306.07837 \[cond-mat.str-el\]](#).
- [34] Viktor Christiansson, Francesco Petocchi, and Philipp Werner, “Correlated electronic structure of $\text{La}_3\text{Ni}_2\text{O}_7$ under pressure,” [arXiv e-prints](#) , [arXiv:2306.07931 \(2023\)](#), [arXiv:2306.07931 \[cond-mat.str-el\]](#).
- [35] Yu-Bo Liu, Jia-Wei Mei, Fei Ye, Wei-Qiang Chen, and Fan Yang, “The s^{\pm} -Wave Pairing and the Destructive Role of Apical-Oxygen Deficiencies in $\text{La}_3\text{Ni}_2\text{O}_7$ Under Pressure,” [arXiv e-prints](#) , [arXiv:2307.10144 \(2023\)](#), [arXiv:2307.10144 \[cond-mat.supr-con\]](#).
- [36] Chen Lu, Zhiming Pan, Fan Yang, and Congjun Wu, “Inter-layer Coupling Driven High-Temperature Superconductivity in $\text{La}_3\text{Ni}_2\text{O}_7$ Under Pressure,” [arXiv e-prints](#) , [arXiv:2307.14965 \(2023\)](#), [arXiv:2307.14965 \[cond-mat.supr-con\]](#).
- [37] Yang Zhang, Ling-Fang Lin, Adriana Moreo, Thomas A. Maier, and Elbio Dagotto, “Structural phase transition, s_{\pm} -wave pairing and magnetic stripe order in the bilayered nickelate superconductor $\text{La}_3\text{Ni}_2\text{O}_7$ under pressure,” [arXiv e-prints](#) , [arXiv:2307.15276 \(2023\)](#), [arXiv:2307.15276 \[cond-mat.supr-con\]](#).
- [38] Yi-feng Yang, Guang-Ming Zhang, and Fu-Chun Zhang, “Minimal effective model and possible high- T_c mechanism for superconductivity of $\text{La}_3\text{Ni}_2\text{O}_7$ under high pressure,” [arXiv e-prints](#) , [arXiv:2308.01176 \(2023\)](#), [arXiv:2308.01176 \[cond-mat.supr-con\]](#).
- [39] Victor Pardo and Warren E. Pickett, “Metal-insulator transition in layered nickelates $\text{La}_3\text{Ni}_2\text{O}_{7-\delta}$ ($\delta = 0.0, 0.5, 1$),” *Phys. Rev. B* **83**, 245128 (2011).
- [40] John P Perdew, Kieron Burke, and Matthias Ernzerhof, “Generalized gradient approximation made simple,” *Physical review letters* **77**, 3865 (1996).
- [41] Richard M Martin, *Electronic structure: basic theory and practical methods* (Cambridge university press, 2020).
- [42] Pedro Borlido, Thorsten Aull, Ahmad W. Huran, Fabien Tran, Miguel A. L. Marques, and Silvana Botti, “Large-Scale Benchmark of Exchange–Correlation Functionals for the Determination of Electronic Band Gaps of Solids,” *Journal of Chemical Theory and Computation* **15**, 5069–5079 (2019).
- [43] Georg Kresse and Jürgen Furthmüller, “Efficient iterative schemes for ab initio total-energy calculations using a plane-wave basis set,” *Physical review B* **54**, 11169 (1996).
- [44] Georg Kresse and Daniel Joubert, “From ultrasoft pseudopotentials to the projector augmented-wave method,” *Physical review b* **59**, 1758 (1999).
- [45] Axel D Becke, “Density-functional thermochemistry. III. The role of exact exchange,” *The Journal of chemical physics* **98**, 5648–5652 (1993).
- [46] John P. Perdew and Karla Schmidt, “Jacob’s ladder of density functional approximations for the exchange-correlation energy,” *AIP Conference Proceedings* **577**, 1–20 (2001).
- [47] Aliaksandr V Krukau, Oleg A Vydrov, Artur F Izmaylov, and Gustavo E Scuseria, “Influence of the exchange screening parameter on the performance of screened hybrid functionals,” *The Journal of chemical physics* **125** (2006).
- [48] John P Perdew, Matthias Ernzerhof, and Kieron Burke, “Rationale for mixing exact exchange with density functional approximations,” *The Journal of chemical physics* **105**, 9982–9985 (1996).
- [49] Matthias Ernzerhof and Gustavo E Scuseria, “Assessment of the Perdew–Burke–Ernzerhof exchange-correlation functional,” *The Journal of chemical physics* **110**, 5029–5036 (1999).
- [50] Carlo Adamo and Vincenzo Barone, “Toward reliable density functional methods without adjustable parameters: The PBE0 model,” *The Journal of chemical physics* **110**, 6158–6170 (1999).
- [51] Philip J Stephens, Frank J Devlin, Cary F Chabalowski, and Michael J Frisch, “Ab initio calculation of vibrational absorption and circular dichroism spectra using density functional force fields,” *The Journal of physical chemistry* **98**, 11623–11627 (1994).
- [52] Jiangang Yang, Hualei Sun, Xunwu Hu, Yuyang Xie, Taimin Miao, Hailan Luo, Hao Chen, Bo Liang, Wenpei Zhu, Gexing Qu, Cui-Qun Chen, Mengwu Huo, Yaobo Huang, Shenjin Zhang, Fengfeng Zhang, Feng Yang, Zhimin Wang, Qinjun Peng, Hanqing Mao, Guodong Liu, Zuyan Xu, Tian Qian, Dao-Xin Yao, Meng Wang, Lin Zhao, and X. J. Zhou, “Orbital-Dependent Electron Correlation in Double-Layer Nickelate $\text{La}_3\text{Ni}_2\text{O}_7$,” [arXiv e-prints](#) , [arXiv:2309.01148 \(2023\)](#), [arXiv:2309.01148 \[cond-mat.supr-con\]](#).
- [53] Arash A Mostofi, Jonathan R Yates, Young-Su Lee, Ivo Souza, David Vanderbilt, and Nicola Marzari, “wannier90: A tool for obtaining maximally-localised Wannier functions,” *Computer physics communications* **178**, 685–699 (2008).
- [54] Nicola Marzari, Arash A Mostofi, Jonathan R Yates, Ivo Souza, and David Vanderbilt, “Maximally localized Wannier functions: Theory and applications,” *Reviews of Modern Physics*

- 84**, 1419 (2012).
- [55] Xiaoyang Chen, Jaewon Choi, Zhicheng Jiang, Jiong Mei, Kun Jiang, Jie Li, Stefano Agrestini, Mirian Garcia-Fernandez, Xing Huang, Hualei Sun, Dawei Shen, Meng Wang, Jiangping Hu, Yi Lu, Ke-Jin Zhou, and Donglai Feng, “Electronic and magnetic excitations in $\text{La}_3\text{Ni}_2\text{O}_7$,” (2024), [arXiv:2401.12657 \[cond-mat.supr-con\]](#).
- [56] Kaiwen Chen, Xiangqi Liu, Jiachen Jiao, Myyuan Zou, Yixuan Luo, Qiong Wu, Ningyuan Zhang, Yanfeng Guo, and Lei Shu, “Evidence of spin density waves in $\text{La}_3\text{Ni}_2\text{O}_{7-\delta}$,” [arXiv e-prints](#), [arXiv:2311.15717 \(2023\)](#), [arXiv:2311.15717 \[cond-mat.str-el\]](#).
- [57] Tao Wu et al. to be appeared, .
- [58] Olivier Parcollet, Michel Ferrero, Thomas Ayral, Hartmut Hafermann, Igor Krivenko, Laura Messio, and Priyanka Seth, “TRIQS: A toolbox for research on interacting quantum systems,” [Computer Physics Communications](#) **196**, 398 – 415 (2015).
- [59] Priyanka Seth, Igor Krivenko, Michel Ferrero, and Olivier Parcollet, “TRIQS/CTHYB: A continuous-time quantum Monte Carlo hybridisation expansion solver for quantum impurity problems,” [Computer Physics Communications](#) **200**, 274 – 284 (2016).
- [60] S. A. Sunshine, T. Siegrist, L. F. Schneemeyer, D. W. Murphy, R. J. Cava, B. Batlogg, R. B. van Dover, R. M. Fleming, S. H. Glarum, S. Nakahara, R. Farrow, J. J. Krajewski, S. M. Zahurak, J. V. Waszczak, J. H. Marshall, P. Marsh, L. W. Rupp, and W. F. Peck, “Structure and physical properties of single crystals of the 84-K superconductor $\text{Bi}_{2.2}\text{Sr}_2\text{Ca}_{0.8}\text{Cu}_2\text{O}_{8+\delta}$,” [Phys. Rev. B](#) **38**, 893–896 (1988).
- [61] Kun Jiang, Ziqiang Wang, and Fu-Chun Zhang, “High-temperature superconductivity in $\text{La}_3\text{Ni}_2\text{O}_7$,” [Chinese Physics Letters](#) **41**, 017402 (2024).
- [62] F. C. Zhang and T. M. Rice, “Effective Hamiltonian for the superconducting Cu oxides,” [Phys. Rev. B](#) **37**, 3759–3761 (1988).
- [63] Piers Coleman, “New approach to the mixed-valence problem,” [Phys. Rev. B](#) **29**, 3035–3044 (1984).
- [64] P W Anderson, P A Lee, M Randeria, T M Rice, N Trivedi, and F C Zhang, “The physics behind high-temperature superconducting cuprates: the ‘plain vanilla’ version of RVB,” [Journal of Physics: Condensed Matter](#) **16**, R755 (2004).
- [65] Kun Jiang, Congcong Le, Yinxiang Li, Shengshan Qin, Ziqiang Wang, Fuchun Zhang, and Jiangping Hu, “Electronic structure and two-band superconductivity in unconventional high- T_c cuprates $\text{Ba}_2\text{CuO}_{3+\delta}$,” [Phys. Rev. B](#) **103**, 045108 (2021).
- [66] Kun Jiang, Xianxin Wu, Jiangping Hu, and Ziqiang Wang, “Nodeless High- T_c Superconductivity in the Highly Overdoped CuO_2 Monolayer,” [Phys. Rev. Lett.](#) **121**, 227002 (2018).
- [67] Zehao Dong, Mengwu Huo, Jie Li, Jingyuan Li, Pengcheng Li, Hualei Sun, Yi Lu, Meng Wang, Yayu Wang, and Zhen Chen, “Visualization of Oxygen Vacancies and Self-doped Ligand Holes in $\text{La}_3\text{Ni}_2\text{O}_{7-\delta}$,” [arXiv e-prints](#), [arXiv:2312.15727 \(2023\)](#), [arXiv:2312.15727 \[cond-mat.supr-con\]](#).
- [68] Zhen Fan, Jian-Feng Zhang, Bo Zhan, Dingshun Lv, Xing-Yu Jiang, Bruce Normand, and Tao Xiang, “Superconductivity in nickelate and cuprate superconductors with strong bilayer coupling,” [arXiv e-prints](#), [arXiv:2312.17064 \(2023\)](#), [arXiv:2312.17064 \[cond-mat.supr-con\]](#).
- [69] Sergei L Dudarev, Gianluigi A Botton, Sergey Y Savrasov, CJ Humphreys, and Adrian P Sutton, “Electron-energy-loss spectra and the structural stability of nickel oxide: An LSDA+U study,” [Physical Review B](#) **57**, 1505 (1998).